Molecular Dynamics Simulation of the Nematic Melt of a *p*-Hydroxybenzoic Acid/2-Hydroxy-6-naphthoic Acid Liquid Crystalline Copolyester

Rishikesh K. Bharadwaj and Richard H. Boyd*

Departments of Materials Science and Engineering and of Chemical and Fuels Engineering, University of Utah, Salt Lake City, Utah 84112

Received July 6, 1998; Revised Manuscript Received August 17, 1998

ABSTRACT: A molecular dynamics simulation has been carried out on a model for the nematic melt phase of a thermotropic liquid crystalline polymer of the Vectra type, a 70/30 random copolymer of *p*-hydroxybenzoic acid (HBA) and 2-hydroxy-6-naphthoic acid (HNA). The periodic simulation box, which contained 12 chains of 10 monomers each, was orthorhombic in shape, and its *a*, *b*, and *c* dimensions could independently adjust under constant pressure. The X-ray scattering pattern calculated for the melt is in good agreement with experimental results. Analysis showed the chains to be highly disordered conformationally in that the dispositions of successive ester group directions and aromatic ring staggers were found to be distributed over all four available positions, at ca. ± 60° and ±120°. Translational register of chains, a feature believed to be present experimentally in the 3D ordered or "crystalline" lower temperature state, is found here to be present also in the nematic melt state. Thus, conformational disorder appears to be the principal distinction between the melt and the lower temperature ordered state. The melt remains in the nematic state on cooling to ambient temperature in the simulations.

Introduction

Structure vs property relationships in liquid crystalline polymers (LCPs) are an area of ongoing interest. These polymers find application as high-performance fibers and moldings. Many of their desirable properties arise from the presence of a high degree of ordering. Although they are of an extended chain nature, they possess characteristics that are common to amorphous and semicrystalline polymeric materials such as the glass−rubber transition and subglass relaxations. One prominent group of such polymers that have received considerable attention is the wholly aromatic random copolyesters of *p*-hydroxybenzoic acid (HBA) and 2-hydroxy-6-naphthoic acid (HNA) known commercially as Vectra. In particular, the three-dimensional structure[1−6] conformational relaxations,[7,8] and transport properties have been studied extensively.[9−12]

A number of molecular modeling and simulation efforts have been carried out on the HBA/HNA polymers in order to gain insight into the structural organization. The connection between X-ray diffraction and monomer ordering has been investigated.[1−3,13] The isolated single chain of the HBA homopolymer has been studied.[14,15] Rotational isomeric state calculations have been applied to the single-chain dimensions of poly-HBA, poly-HNA, and the random copolymers.[16] The high-temperature phases and transitions in crystalline HBA homopolymer have been investigated via Monte Carlo (MC) techniques.[17] The ordering in bulk liquid crystalline (LC) phases of rigid models for the dimer and tetramer of HBA has been studied.[18,19] The packing in the 70/30 random copolymer has been investigated via molecular mechanics energy minimizations.[20] The structure of a regularly alternating 1/1 HBA/HNA copolymer has been studied using MC simulation.[21]

In the present work we have undertaken a molecular dynamics (MD) simulation of the bulk 70/30 HBA/HNA random polymer. Because, as discussed in more detail in the next section, the copolymers are morphologically complicated and behave much like two-phase crystalline/amorphous systems, the goal here is a simplified one. It is to generate and study the high-temperature nematic melt. In addition, the glass formed by cooling the melt is investigated.

To accomplish the above, it is necessary to create a simulation assembly that contains chains long enough to accommodate the random copolymer concept and sufficient chains to create a suitable packing environment. The simulation is carried out in the constant pressure (*P*), temperature (*T*), and particle number (*N*) ensemble (*NPT*). This allows the *a*, *b*, and *c* dimensions of the orthorhombic periodic simulation box to independently adjust under constant-pressure conditions. The stability of the LC ordering is thus addressed. This also allows volume-temperature (*V*−*T*) relations to be studied. The latter point is in keeping with the philosophy adopted in previous simulations,[22−26] where the *V*−*T* properties have been generated.

Morphology of HBA/HNA Copolymers

At this point it is appropriate to briefly review some aspects of the morphology of the HBA/HNA polymers. It is, of course, fundamental that the polymers can form a nematic liquid crystalline state. However, the situation is complicated by the presence of transitional phenomena within the LC state. In both the 70/30 and 58/42 polymers[4,27] a differential scanning calorimetry (DSC) transition occurs on heating at ∼550 K. Displacement of the transition on cooling[4] to ∼470 K is suggestive of the undercooling associated with crystallization. The high-temperature state has a diffuse X-ray pattern associated with it. On cooling, sharper peaks appear in powder and fiber patterns superposed over the diffuse pattern. To some degree, slow cooling and annealing enhance the sharpness of the patterns. The above facts are suggestive of a two-phase system at

* To whom correspondence should be addressed.

10.1021/ma9810565 CCC: $15.00
Published on Web 10/10/1998

lower temperature containing both a residual nematic phase and a "crystalline" one. However, several considerations indicate the analogy with semicrystalline polymers is not a complete one. The heat and volume of transition are exceedingly small.[4,27] More fundamentally, a description of the state of order in the more ordered phase that encompasses the random copolymer structure is required.

X-ray fiber patterns at ambient temperature on drawn specimens show several features. Among these are a series of meridional reflections that are aperiodic and not orders of a single repeat. In general, these depend on the copolymer composition, but a reflection at $d = 2.1$ Å is common to them all. Equatorial reflections ($d = 4.5$ Å) indicate the interchain spacing of the bundled parallel chains, but the presence of substantial arcing and off-equatorial reflections indicates some degree of *three*-dimensional ordering. That is, a translational register among the chains exists. At higher temperature, above the disordering transition, the X-ray reflections are much more diffuse. The study of Butzbach et al.[4] on 58/42 HBA/HNA shows the presence of the aperiodic meridional reflections. However, the equatorial and off-equatorial layer lines appear to be too diffuse to resolve, if the latter are present.

Interpretation of these features has been the subject of considerable effort. The aperiodic meridional features can be reproduced from the transform of a random sequence of monomer residues in a single chain. The meridional reflection at a d spacing of 2.1 Å has been associated with the coincidence of the third order of HBA and the fourth order of HNA. Modeling translational registration requires studying packing and is thus more complicated. Hanna and Windle[13] proposed that groups of specific monomer sequences tend to segregate to form domains. Blackwell and co-workers in a series of papers[1−3,20] culminating in a molecular mechanics model of energy-minimized arrays of chains[20] concluded that the translational register is sufficient in random copolymers, without selection of specific sequence matchups, to give rise to the off-equatorial reflections.

In the present simulation, we concentrate on the structure and organization of the high-temperature melt phase and on the effects of cooling it. In MD simulations of crystallizable polymers, the nucleation and growth requirement generally prevents formation of the ordered phase, and vitrification is usually the observed result. This is found here as well.

Simulation Methodology

System Studied. In a representation of the 70/30 copolymer of *p*-hydroxybenzoic acid and 2-hydroxy-6-naphthoic acid, 12 chains of 10 monomeric units each were chosen. The monomer composition of each chain was the same as the bulk system, seven benzoic acid and three naphthoic acid units. They were concatenated in a different random sequence in each chain. The fixed-chain composition was necessary in order to accommodate the chains in a periodic simulation box. All atoms including hydrogens were explicitly included. The above configuration results in 148 atoms/chain, which leads to a total of 1776 atoms/simulation box.

Initial Configuration. A pair of connected HBA and HNA monomer units is depicted in Figure 1. Of the three torsional angles shown, only φ_3 is believed to contribute substantially to the conformational state of the chain. That is, the barriers for maintaining planarity at the aromatic ester (ϕ_1) torsion and ester group (ϕ_2) torsion are substantial. Successive aromatic residues are believed to be alternately staggered at ϕ_3 = ca. ±60°. While the precise angle of stagger between the planes of the successive aromatic rings is not known experimentally with great certainty, X-ray diffraction studies on related molecules such as phenyl benzoate[28] and numerous molecular mechanics and semiempirical quantum chemistry calculations,[29−31] indicate that the angle is approximately 60°. The stagger of the rings, however, does not define the chain conformation. This is because there are four stable positions at ϕ_3, i.e., ±60° and ±120°, and the phenyl ring positions are degenerate with respect to 180° rotations from these positions. A conceptually more transparent way to monitor the chain conformation is to create a "virtual" bond across an aromatic ring that connects an ester sp^2 carbon and the next main-chain ester oxygen.[16,26,32] It is convenient to base the torsional angle of the virtual bond on main-chain atoms and thus on the following sequence: ester carbon, ester main-chain oxygen, ester carbon, ester main-chain oxygen. This virtual bond is collinear with the connecting bonds to the rings in the phenyl rings but only approximately so in the naphthyl rings. In the virtual bond representation, the chain conformation is defined by the virtual bond torsional angle and ester group torsional angle, ϕ_2 (see Figure 2). The virtual bond ±60° and ±120° conformations arise from the repulsions between the aromatic ring and the ester carbonyl when the ϕ_3 bond is planar at 0° (cis) and 180° (trans). Thus, the approximately ±60° angles are labeled here as distorted by rotation through a positive or negative angle from cis as $c^+ = \sim 60°$ and $c^- = \sim -60°$ and the ±120° angles as distorted by rotation from trans as $t^- = \sim 120°$ and $t^+ = \sim 240° = \sim -120°$. The ester group ($\phi_2$) torsion remains at trans in all conformations and is labeled as T. In this notation there are two extended conformations of the chain having a regularly repeating torsional angle sequence. These are .../Tc^+/Tc^-/... and .../Tt^+/Tt^-/..., where the slashes indicate partition into monomeric units. The conformations are illustrated in Figure 2 for the case of HBA homopolymer. It is to be noted (see the end views in Figure 2) that a virtual bond conformation sets the angle between the projections of successive ester group directions (as determined by the carbonyl bond) and therefore also the staggering of the aromatic rings.

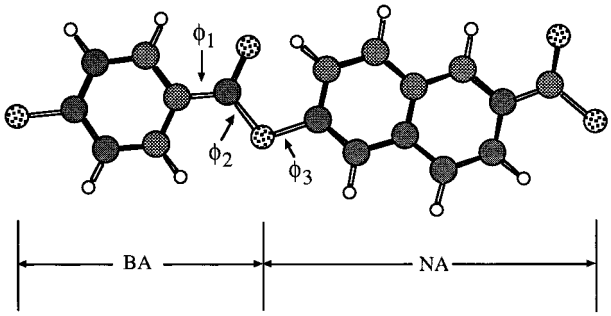

Figure 1. Representation of *p*-hydroxybenzoic acid (HBA) and 2-hydroxy-6-naphthoic acid (HNA) monomer units showing definitions of the torsional angles.

The chains used to fill the initial periodic box below were in the .../Tt^+/Tt^-/... conformational sequence.

Highly oriented drawn fibers of the 70/30 polymer give rise to X-ray diffraction patterns that can be interpreted in terms of quasi-orthorhombic crystal pack-

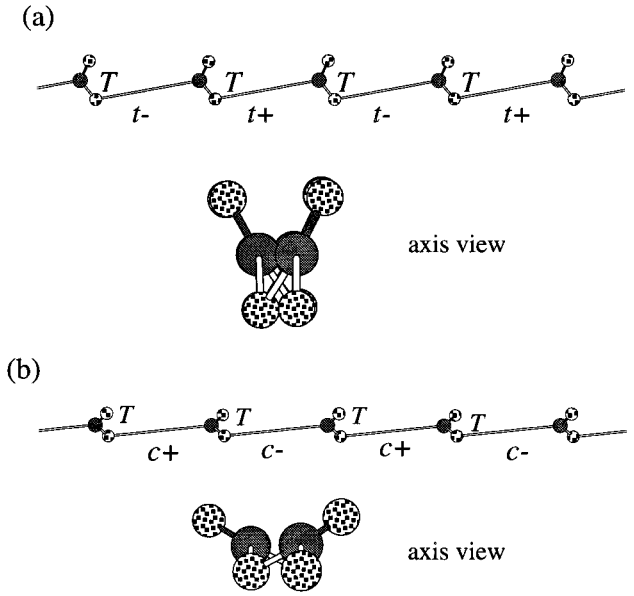

Figure 2. Virtual bond representation of the chain conformation. The ester groups are planar and in the trans (*T*) conformation. Two extended conformations are shown. In part a the virtual bonds spanning the aromatic rings are shown as alternating between the two distorted from trans states t^- and t^+ (∼120°, ∼−120°). In part b the virtual bonds alternate between the two distorted from cis states c^+ and c^- (∼60°, ∼−60°). The ester group carbonyl bonds are the dark filled bonds in the axis views.

ing with two chains per cell.[1] The basal plane dimensions are $a = 9.18$ Å and $b = 5.3$ Å. This structure was used to create a starting periodic simulation box that contains 12 chains arranged in an orthorhombic array; see Figure 3. The resulting initial dimensions of the box were $a = 18.4$ Å, $b = 15.9$ Å, and $c = 75$ Å. The dimension of the box in the chain direction, *c*, was arbitrarily fixed, ensuring that the ends of the chains and their periodic images were sufficiently far apart to prevent unfavorable nonbonded repulsion. However, since the cell edges are free to evolve and fluctuate during the MD simulation under the forces arising from the energy model and the applied pressure, the precise values accorded to the simulation cell in the initial stage are not crucial.

Molecular Dynamics Simulation. All of the MD simulations were performed in the *NPT* ensemble. The velocity[33] form of the Verlet[34] algorithm was utilized in integrating Newton's equations of motion. Temperature and pressure control was achieved by using the Berendsen weak coupling algorithm.[35] The velocities are scaled by a temperature-scaling parameter (λ), while the coordinates and the box dimensions are scaled by the pressure-scaling parameter (χ) at each MD step. The temperature-scaling parameter is given by

$$\lambda = \left\{1 - \frac{\delta t}{t_T}\left(1 - \frac{T_0}{T}\right)\right\}^{1/2} \quad (1)$$

where δt is the time step and τ_T is the temperature coupling constant, which controls the rate at which the target temperature T_0 is achieved and the degree of fluctuation of the instantaneous temperature *T* from the target temperature. The pressure-scaling parameter is given by

$$\chi = 1 - \zeta_P \delta t(P_0 - P) \quad (2)$$

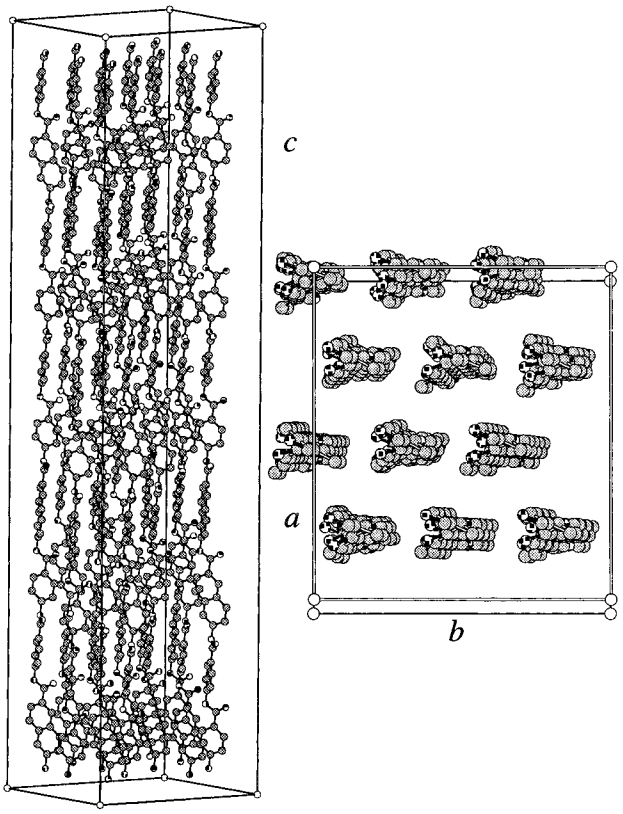

Figure 3. Initial configuration of the system of 12 chains as arranged in an orthorhombic periodic simulation cell. Hydrogen atoms are blanked for clarity.

where ζ_P is the pressure coupling constant and *P* and P_0 are the measured and desired system pressures, respectively. The temperature and pressure coupling constants were chosen to be 1 fs and 10^{-7} (s atm)$^{-1}$, respectively. This choice of value for the pressure coupling constant gave acceptable fluctuations in the volume and at the same time resulted in reasonably fast equilibration of the system to the target pressure. Lower values for ζ_P and τ_T resulted in divergence of the time integration from a classical trajectory, while higher values yielded very long equilibration times. The MD time step was 1 fs.

The simulations were conducted using an orthorhombic periodic cell as described above. This is a straightforward extension of the cubic case with only the added requirement of applying the periodic boundary conditions with respect to each cell vector separately. Use of the orthorhombic periodic cell results in the monitored pressures in the three directions being unequal and hence results in the principal diagonal elements of the pressure tensor being unique. The case is simplified due to the orthogonal symmetry which causes nondiagonal elements of the tensor to vanish. The pressure is controlled separately in each of the three directions which is realized by keeping track of the forces in each of the three directions and computing the diagonal components of the pressure tensor as formulated atomistically.[36] All of the forces on each atom were used. With this accomplished, the scaling of the coordinates and the cell dimensions by the pressure-scaling parameter is carried out. In principle, the pressure-scaling parameter (eq 2) is also a tensor of the same rank as the pressure tensor. However, in this study, the pressure coupling constant ζ_P was set to the same value in each of the three directions, while the scaling factor χ

Table 1. Valence Potential Functions[a]

Bond Stretching Energy = $^1/_2\, k_R(R - R_0)^2$

bond type	k_R[b]	R_0
O−CA[c]	663 (4.4)	1.42
CA−CA[d]	1152 (7.6)	1.39
CA−HA[d]	663 (4.4)	1.09
CA−CD[c]	663 (4.4)	1.49
O−CD[e]	783 (5.2)	1.33
CD−OD[e]	1431 (9.5)	1.22

Bond Bending Energy = $^1/_2 k_\theta(\theta - \theta_0)^2$

angle type	k_θ[f]	θ_0 (deg)
O−CA−CA[c]	422 (0.7)	120.0
CA−CA−CA[d]	603 (1.0)	120.0
CA−CA−HA[c]	302 (0.5)	120.0
CA−CA−CD[c]	422 (0.7)	120.0
OD−CD−CA[e]	603 (1.0)	124.0
O−CD−CA[e]	1024 (1.7)	110.5
OD−CD−O[e]	603 (1.0)	120.0
CA−O−CD[e]	422 (0.7)	109.47

Torsional Energy = $^1/_2 V_\phi(1 + C\cos(N\phi))$

torsional type[g]	V_ϕ	C	N
O−CA−CA−CA[c]	180	1	1
CA−CA−CA−CA[d]	108	−1	2
CA−CA−CA−CD[c]	108	−1	2
CA−CA−CA−HA[c]	66	−1	2
O−CD−CA−CA[c]	58	−1	2
CA−O−CD−CA[e]	58	−1	2
CA−CA−O−CD[h]	12.5	−1	2

Out-of-Plane Bending Energy = $^1/_2 k_\delta \delta^2$

out-of-plane type[i]	k_δ
OD* CA−CD−O	361

[a] Energies are in kJ mol^{-1}, distances in Å, and angles in rad (shown above as deg). The notation is as follows: HA = aromatic hydrogen; CD = sp^2 carbon; CA = aromatic carbon; O = divalent oxygen; OD = carbonyl oxygen. [b] The values in parentheses are in classical spectroscopic units of mdyn Å^{-1} and *not* divided by 4 for MD simulation purposes. [c] Reference 37. [d] Reference 22. [e] Taken to be the same as corresponding values in ref 38, with the aromatic carbon where it appears above replaced by an aliphatic carbon. [f] The values in parentheses are in classical spectroscopic units of mdyn Å. [g] Only one torsional term per bond was set up. In the case of multiple choices for the end atoms in the three-bond sequence, only one was selected. [h] Adjusted in this work to give, when used with the nonbonded functions adopted, a staggering of the aromatic residues in the vicinity of ±50°. [i] Deformaton of the carbonyl oxygen from the plane of the other three centers; the value of ref 38 was increased by a factor of $^5/_3$.

was computed separately for each principal diagonal pressure tensor component.

The simulations were initially conducted at 560 K, and lower temperature systems were created from this sample by cooling in 25 K intervals, with a minimum of 400 ps allowed to elapse between each temperature change to allow the system to equilibrate. Volume equilibration was judged by the volume attaining a constant value with time and was monitored over time periods between 1 and 5 ns at different temperatures.

The computations were carried out on IBM RS6000/560 or /370 workstations using the IBM MASS (2.2) mathematical acceleration library and SUN ULTRA 170E workstations. The CPU time taken per step was 0.5 s on the IBM 370, while it was 0.27 s on the SUN ULTRA.

Force Field. The valence potential functions and the constants used are listed in Table 1. The functions, with one exception discussed below, were taken or adapted from the database MOLBD3[37] and from earlier studies[22,38] as detailed in the footnotes to the table. The bond stretching constants were diminished from the original spectroscopic values by a factor of 4 in order to increase the time step. Also the mass of the hydrogen atoms was increased by a factor of 2 (perdeuterated polymer). Well-behaved trajectories were obtained at a time step of 1 fs.

Table 2. Nonbonded and Electrostatic Energy Parameters[a]

Nonbonded Energy[b] = $A\exp(-BR) - C/R^6$

atom type[c]	$A \times 10^{-4}$	B	C	R_{min}	σ	ϵ
O···O	31.74	4.063	1669.4	3.20	2.85	0.837
C···C	6.267	3.090	2681.7	3.872	3.45	0.396
C···H	1.808	3.415	578.4	3.274	2.89	0.217
H···H	1.109	3.740	114.7	3.37	3.0	0.0410

Electrostatic Energy = $q_i q_j/(4\pi\epsilon_0\epsilon' r_{ij})$

$\epsilon' = \epsilon_B \exp(-a_c r_{ij}^{-1} \ln \epsilon_B)$

Switching Polynomial,
$S = 1 - (3r_t - r_\epsilon - 2r_{ij})(r_{ij} - r_\epsilon)^2 (r_t - r_\epsilon)^{-3}$

ϵ_B	a_c (Å)	r_t (Å)	r_ϵ (Å)
4.5	3.45	7	2.7

atom type	q[d]
CD	0.333e
OD	−0.270e
O	−0.126e
CA	0.063e

[a] Energies are in kJ mol^{-1} and distances in Å. [b] The nonbonded functions are independent of the atom hybridization; i.e., double- and single-bonded oxygens are the same, and aromatic and ester carbons are the same. [b] R_{min} is the distance at the minimum, ϵ is the well depth, and σ is the distance at which energy is zero. The potential constants are from ref 39. [c] The C···H potential is given explicitly, but the C···O and O···H potentials are constructed from the geometric mean for A and C and the arithmetic mean for B. [d] The charges are expressed as fractions of the absolute value of the electronic charge, e, from ref 38.

The nonbonded interactions are of the exponential-6 form. Their constants were taken from previous work[39] and are listed in Table 2. Interactions were invoked between four-center (three-bond) and higher separations. The nonbonded interactions were truncated at a radius of 7 Å. This truncation radius was occasioned by the requirement of being less than half the dimension of the periodic box in the smallest (b) direction, ∼15 Å. Long-range pressure and energy correction terms were explicitly taken into account. Formulations for the isotropic continuum case[36] could be used since the nonbonded cutoff radius was large enough that the various atom type pair distribution functions had approached unity at this point.[40]

As indicated above, the orientation of the planes of the aromatic units relative to each other is the most important conformational feature of the chain. This is determined by the values of the torsional angle ϕ_3 in Figure 1. The equilibrium value of the torsional angle is the result of the interplay between the intrinsic torsional potential at this bond and the repulsive nonbonded five- and six-center steric interactions between the carbonyl oxygen and the aromatic C−H unit situated α to the attaching aromatic carbon in the adjacent ring. The 2-fold intrinsic potential barrier V_ϕ of type CA−CA−O−CD in Table 2 was determined by adjustment in order to give a stagger angle in the vicinity of ±60°. If the value of the barrier is low, no stable minima appear near these positions, only maxima

at 0 and 180°. High values of the barrier lead to smaller splittings and eventually to only maxima at ±90°. The actual value obtained for the angle is somewhat ambiguous as it has to be determined by sampling and thus depends somewhat on the conditions of the latter. At low temperature, in the bulk, the value chosen gives sampled values of ca. ± 50°.

Electrostatic effects were incorporated via partial charges located at the polar atoms. These were regarded to be the ester group carbon and two oxygens as well as the aromatic carbon connected to the divalent ester oxygen. Polarization effects were incorporated via the distance-dependent dielectric constant method,[41−44] in which the electrostatic energy is written as

$$U(r_{ij}) = \frac{1}{4\pi\epsilon_0}\sum_{i<j}\frac{q_i q_j}{\epsilon_d(r_{ij})r_{ij}} \tag{3}$$

where the q's are the charges, r_{ij} is their separation, ϵ_0 is the permittivity of free space, and $\epsilon_d(r_{ij})$ is the (relative) distance-dependent dielectric constant. The distance dependence of the dielectric constant is based on the representation

$$\epsilon_d(r_{ij}) = 1, \qquad r_{ij} < a_c$$

$$= \epsilon_B \exp\left(-\frac{a_c}{r_{ij}}\ln(\epsilon_B)\right), \qquad r_{ij} > a_c \tag{4}$$

where a_c is a radius below which screening is judged not to take place with the dielectric constant remaining at unity and beyond which it is accounted for by Debye screening that smoothly approaches the bulk dielectric constant, ϵ_B, at large distances. The screening limit a_c was adopted as a typical contact distance and taken to be that between carbon centers (σ_{C-C}, Table 2) with the value 3.45 Å. The bulk constant ϵ_B was taken to be 4.5.[7,8] In practice, these equations can be approximated by fitting a switching polynomial to eq 3 (with eq 4 embedded).[43,44] The polynomial, and thus the force, has the property of going smoothly to zero at the truncation radius, r_t. It takes on the value unity at an arbitrary switching radius, r_ϵ, and is given by

$$S(r_{ij}) = 1 - \frac{(3r_t - r_\epsilon - 2r_{ij})(r_{ij} - r_\epsilon)^2}{(r_t - r_\epsilon)^3} \tag{5}$$

The electrostatic energy is taken relative to a zero at the truncation radius by writing the individual terms as

$$\Delta U^0_{ij} = \frac{q_i q_j}{4\pi\epsilon_0}\left(\frac{1}{r_{ij}} - \frac{1}{\epsilon_B r_t}\right) \tag{6}$$

The complete energy is then

$$U_{ij} = \Delta U^0_{ij}, \qquad r_{ij} < r_\epsilon \tag{7a}$$

$$U_{ij} = \Delta U^0_{ij} S(r_{ij}), \qquad r_\epsilon \le r_{ij} \le r_t \tag{7b}$$

$$U_{ij} = 0, \qquad r_{ij} > r_t \tag{7c}$$

The truncation radius r_t is fixed a priori at some suitably large distance. In our case, it is taken to be the same as the nonbonded truncation radius, 7 Å. The switching radius, r_ϵ, is determined by adjustment to optimize the agreement of eq 7 with eqs 3 and 4. For $a_c = 3.45$ Å, $\epsilon_B = 4.5$, and $r_t = 7$ Å, the best agreement was obtained for $r_\epsilon = 2.7$ Å. The values of the partial charges were taken from an earlier study.[38] The electrostatic parameters are collected in Table 2.

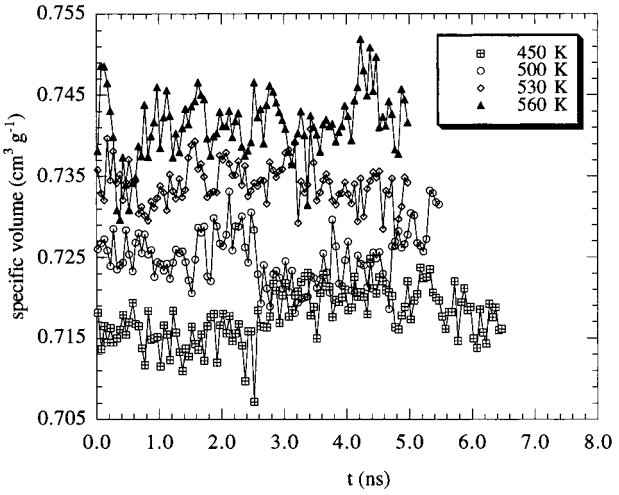

Figure 4. Specific volume vs time at several temperatures. The points are 50 ps averages.

Results and Discussion

Equilibration. The equilibration of specific volume with time is displayed in Figure 4 for several different temperatures as obtained from *NPT* simulations. The specific volume typically achieved equilibration over periods of about 200 ps. This is acceptably rapid. It is presumed to some degree to be aided by the circumstance that the volume is dominated by the lateral packing of extended chains, which in turn is effected by rearrangements of the phenyl and naphthyl rings driven by fairly rapid conformational transitions at the ϕ_3 bond connections[7,8] (see Figure 1).

Another measure of the equilibration of the system is the extent to which the chains are capable of utilizing translational motions, along the *c* direction, in optimizing the packing in the system. That is, it is to be hoped that the translational registration between chains along this direction should be established by accessibility of configuration space in the simulation and not imposed by the initial configuration of the system. This point was investigated by sampling the translational positions of the chains. Since the *NPT* cell dimension fluctuations, especially in the *c* dimension (cf. Figure 4 and thermal expansion results below), are quite small compared to the level of translational movements being investigated, the cell ends are a convenient marker to record the translational positions. The positions of the start and end of each chain relative to the bottom and top, respectively, of the periodic box ($Z = 0$, c) were determined. The results of sampling at two temperatures are displayed in Figure 5. It may be seen that substantial displacements over the sampling interval, on the order of several angstoms at high temperature, are observed. This would appear to be sufficient to indicate participation of this degree of freedom in finding favorable local packing. However, it is also to be noted that these displacements are insufficient to explore the question of the domain segregation suggested by Hanna and Windle[13] even if the cell were large enough to encompass enough chains to make the quest meaningful.

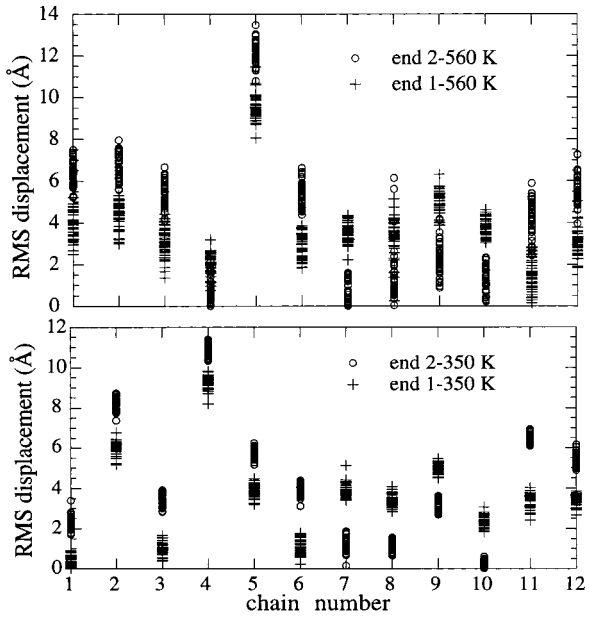

Figure 5. Translational configurational space exploration. The absolute value of the displacement from the box ends of the chain ends at various sampling points. There are 40 sampling points over 10 ns at 560 K and 10 points over 1 ns at 350 K.

A snapshot of the simulation at 500 K is shown in Figure 6. As is evident, although there is a high degree of local conformational disorder along the chains, they remain extended in a manner consistent with the nematic liquid crystalline state.

Volume-Temperature Results. The time-averaged specific volume of the system is presented at a number of temperatures in Figure 7. The specific volume of the system at 298 K was found to be 0.684 $cm^3\ g^{-1}$, and an experimental value of 0.714 $cm^3\ g^{-1}$ is consistent with a number of studies.[7,8,10] Although the agreement is not particularly impressive compared to some previous simulations,[22−26] it should be noted, as indicated in the Simulation Methodology section, that the present one is almost completely based on previously developed force-field parameters. No calibration of the nonbonded potential energy functions was carried out. Thus, in this respect the present simulation is purely predictive in nature, and the agreement can be considered adequate for the purpose at hand.

As will be seen below, there is no structural evidence for the appearance of the ordered or crystalline phase on cooling. However, it is of interest to consider indications of a glass transition in the supercooled nematic phase in the $V-T$ results. In some previous simulations,[22−25] it has been possible to locate a break in the $V-T$ curve indicative of the MD volumetric glass transition. From DSC the experimental value for 70/30 copolymer is ∼370 K.[27] The results in Figure 7 do show upward curvature, and a slightly better fit to the MD data is obtained with a second-order polynomial. However, aside from noting that there is considerable scatter in the MD points in the region 400−450 K, it appears that there is no reasonable basis upon which to locate a definite break. From analysis of conformational dynamics, a subject to be taken up in a separate publication, it is clear that the system behaves on cooling in a typical vitrifying manner and that at 298 K it has the characteristics of a glass.

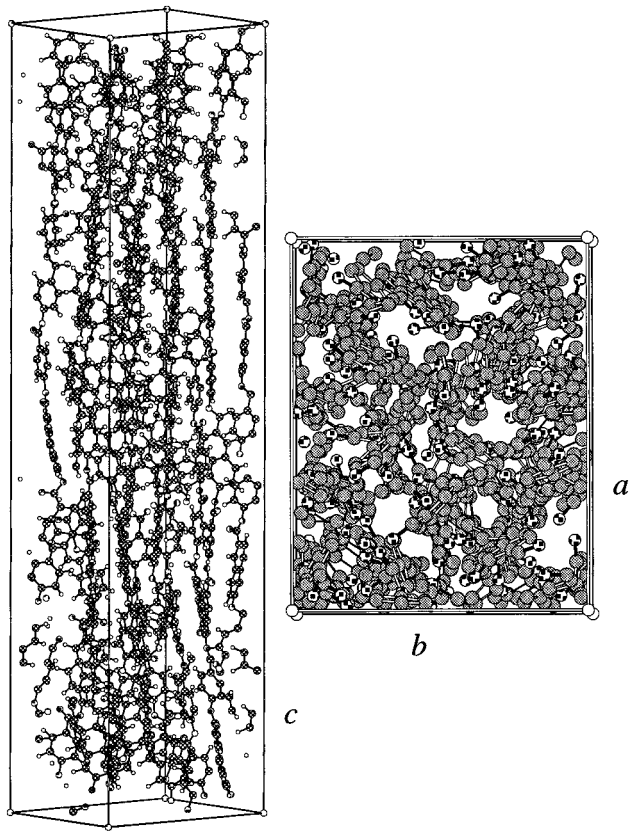

Figure 6. Snapshot of a MD-generated configuration of HBA/HNA copolymer at 500 K. Hydrogen atoms are blanked out for clarity. (The apparent loose atoms are a visualization artifact due to clipping at the periodic box boundaries.)

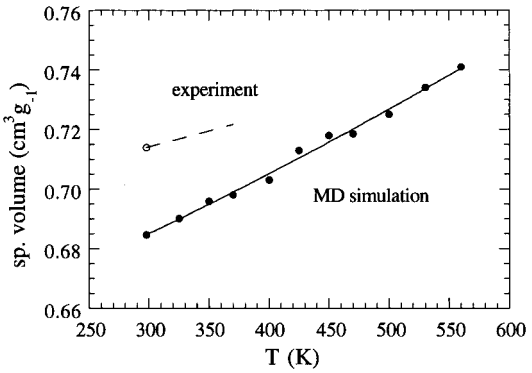

Figure 7. Average specific volume vs temperature at 1 atm of pressure. The filled points are from MD simulation. The circle is from experiment,[7,8,10] and the dashed line is based on experimental thermal expansion data on bulk specimens[45] and crystal X-ray reflections.[46]

The volumetric thermal expansion coefficient from simulation is found from the results of Figure 7 to be $2.8 \times 10^{-4}\ K^{-1}$ at 300 K. An experimental value, near room temperature, of $1.5 \times 10^{-4}\ K^{-1}$ has been reported from the density of bulk specimens,[45] and the same value is reported from X-ray diffraction measurements on the crystalline phase.[46] As expected, as seen in Figure 8, the main contribution to the volumetric coefficient of expansion is from the expansion in the *a* and *b* directions. The X-ray diffraction measurements on the crystalline phase show that the coefficient in the *a* direction is much larger than that in the *b* direction.[46] In contrast, they are found to be similar here in the simulations performed on the cooled melt (Figure 8).

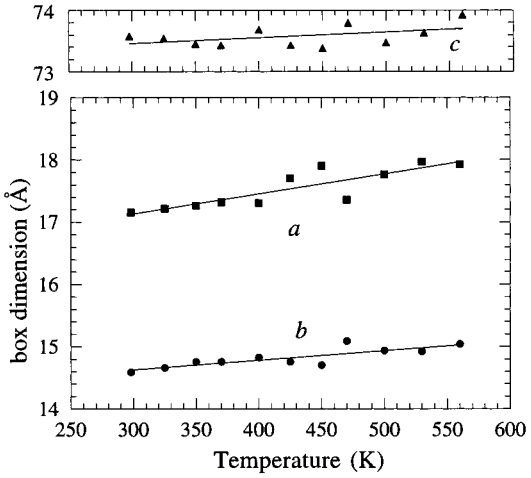

Figure 8. Periodic simulation box dimensions vs temperature.

This is a consequence of the *a*, *b* directional distinction largely disappearing in the melt in simulation (Figure 6) and the situation being maintained on cooling. The higher value found in the *b* direction also appears to account for the higher overall value for the volumetric coefficient of expansion of the cooled melt compared to the crystal phase.

Solubility Parameter. The solubility parameter was calculated at 298 K and found to be 13.2 (cal $cm^{-3})^{1/2}$. The parameter was calculated by taking the cohesive energy density as the sum of the intermolecular nonbonded and Coulombic energies. No direct experimental data for the solubility parameter are available. However, an estimate can be made from group contribution methods. Values for the group volume and the cohesive energy tabulated by van Krevelen[47] and Porter[48] yielded a value of 13.5 (cal $cm^{-3})^{-1/2}$, which compares favorably with the simulation value.

X-ray Scattering Profile. From the discussion on morphology earlier, it is obviously of importance to make a comparison of the X-ray diffraction derived from the simulation results with the experimental ones. To this end, the spherically symmetric powder pattern scattering intensity was calculated from the atom−atom pair distribution functions. The functions for all of the atom pairs are available elsewhere.[40] Standard techniques as discussed by Wagner[49] and invoked previously[22,26] were used. The atomic scattering functions are from Alexander.[50]

The X-ray scattering profiles computed from simulation results at 560 and 298 K are shown in Figure 9. Two features are observed in the simulation results at both temperatures: the diffuse peak from the equatorial reflections due to lateral packing at ∼4.5 Å and the weaker meridional peak due to the third-order HBA and fourth-order HNA reflections. Experimental values of the peak positions are shown as well.[1,46] The equatorial positions are consistent with both the simulation density and the thermal expansion coefficient being somewhat higher than experimental values. The meridional peak is in good agreement with experiment.

Also shown in Figure 9 is an experimental wide-angle powder pattern for a 58/42 HBA/HNA copolymer in the melt[4] that shows the diffuse peak in the equatorial region. It may be seen that the shape found in the simulation is very similar to that observed experimentally.

A significant feature of the X-ray profile at 298 K is that it is representative of experimental and simulation

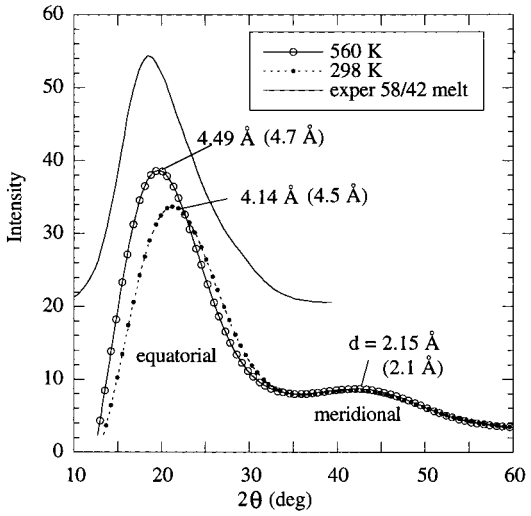

Figure 9. X-ray scattering intensity (powder pattern) vs scattering angle (Cu Kα) at 560 and 298 K as obtained from simulation. The *d* spacings at the peaks are indicated. The numbers in parentheses are experimentally determined *d* spacings, the value alongside the equatorial peak at 560 K is for the ordered phase at 533 K,[46] and the others are for the ordered phase at room temperature.[1] An experimental result for a 58/42 HBA/HNA polymer[4a] is also shown as the curve without points. It has been shifted upward for clarity.

profiles at high temperature, above the disordering transition and therefore in the wholly nematic phase. There is no evidence in the low-temperature simulation results of the superposition of sharper peaks characteristic of the more ordered phase over the diffuse profile of the residual nematic phase. This is to be expected since, as discussed above, experimentally the appearance of the ordered phase on cooling has some of the characteristics of a nucleation and growth process similar to crystallization. In general, observation of such processes is difficult in MD simulations that involve cooling from higher temperature, as was done in generating the simulation results. Thus, the room-temperature simulation structure is that of a supercooled nematic LC phase.

Order Parameter. The liquid crystalline state is characterized by the order parameter, which is a measure of the degree of orientational ordering defined as

$$S = \frac{1}{2}\langle 3\cos^2\theta - 1\rangle \qquad (8)$$

where θ is the angle between the direction of preferred orientation and the long principal axis of the molecule. This function can have a value between 1, indicating parallel alignment, and −0.5, indicating perpendicular alignment. The brackets symbolize ensemble averaging. The order parameter was calculated by using the principal axis, about which the moment of inertia was a minimum. It was found to deviate only slightly from unity in the simulations performed. An experimental value of 0.81 has been reported from X-ray diffraction for 58/42 HBA/HNA copolymer.[4] It is important to note that the latter value responds to the alignment of mesoscopic domains as well as to the ordering within the domains and thus is expected to be less than that for the value of the single domain to which the simulation corresponds.

Conformational Behavior. It is of interest to explore the structure of the nematic melt phase in terms

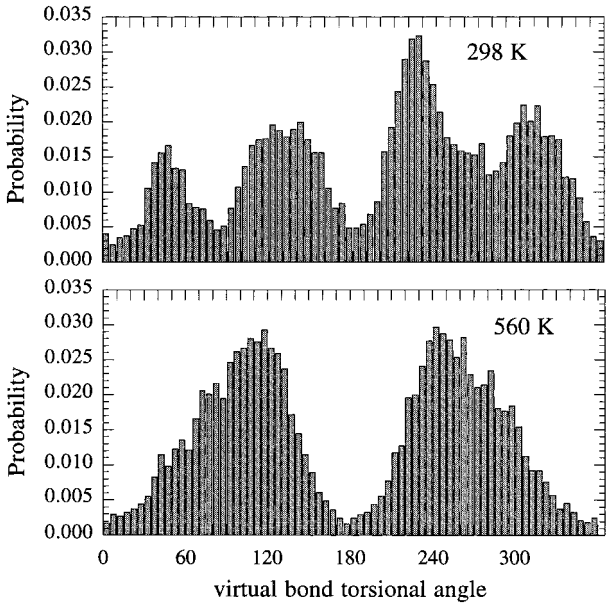

Figure 10. Virtual bond (Figure 2) population, expressed as a normalized probability, at 560 and 298 K (10 ns sampling at 560 K and 2 ns at 298 K).

of chain conformations and packing. Of special importance is the degree to which the chains are intramolecularly disordered. A convenient way to address conformational disorder is in terms of the states of the virtual bonds described above (Figure 2). As indicated earlier, the initial simulation box was set up with conformationally regular extended chains in the repeated Tt^+/Tt^- sequence. The system was sampled to determine the virtual bond states after equilibration. Results for the virtual bond torsional angle populations at 560 and 298 K are shown in Figure 10. At 560 K, there is no clear resolution in the populations of c^+,t^- or c^-,t^+ states and a single peak on either side of 180° is observed. This is due to a very low effective barrier separating these states. The *t* region is slightly favored over the *c* region, by about 60/40. At 298 K, the *t,c* states are now well-resolved and the *t* state is still slightly favored. There is some asymmetry with respect to 180°, but this may be a statistical sampling artifact associated with the fewer transitions among states at lower temperature.

From the above, it is apparent that the chains are highly disordered conformationally. A further question arises as to whether there is any tendency for chains to maintain the alternating staggering of the virtual bond conformations that was included in the starting system. This is addressed by means of plots of the conformation of a given bond against the conformation of the succeeding bond. Such a plot for 560 K is shown in Figure 11 and that for 298 K in Figure 12. If the alternating character were maintained, there would be some favoritism for the lower right and upper left quadrants of the plots. There appears to be no such tendency at 560 K in Figure 11. At 298 K, in Figure 12, the resolution of the populations into *t,c* states noted in Figure 10 is apparent, as is the tendency toward favoring the >180° angles. However, there does not appear to be a tendency toward alternation. The same conclusion prevails with respect to alternation of the staggering of the aromatic rings with respect to each other. Alternation does not prevail in the high-temperature or supercooled nematic melt.

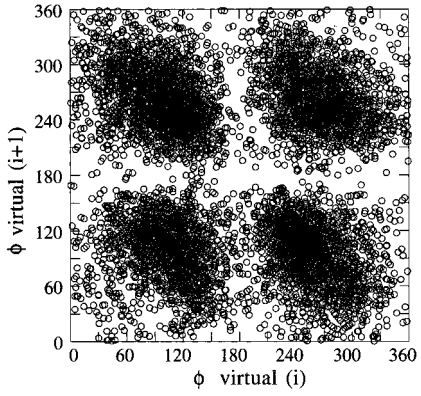

Figure 11. Alternation of virtual bond conformations and, therefore, ester group orientation and alternation of aromatic ring stagger, 560 K. Displayed by plotting individual values of pairs of successive virtual bonds, $\phi(i)$, $\phi(i+1)$, from the same sampling as in Figure 10. Alternation or staggering would have been apparent as emphasis on the upper left and lower right quadrants.

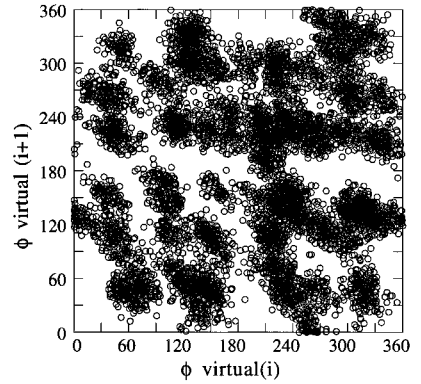

Figure 12. Alternation of virtual bonds and, therefore, ester group orientation and alternation of aromatic ring stagger, 298 K; see Figure 11.

Translational Register among Chains. As indicated in the discussion on morphology earlier, X-ray diffraction on oriented specimens below the ordering transition shows the presence of three-dimensional order, which implies the presence of an intermolecular translational register. The occurrence of registration in the melt was investigated here. A distribution function that records the *c* axis or *Z* positions of ester carbon atoms relative to that of a selected ester carbon was constructed for all ester−ester pairs. The function from sampling at 560 and 298 K is displayed in Figure 13. At 560 K, the function is seen to be strongly alternating, with the phase centered with the maximum at $Z = 0$. The positional interval of the single broad peak corresponds to a weighted average of the HBA and HNA unit lengths. At 298 K splitting into separate peaks for HBA and HNA units is observed. At both temperatures it is evident that considerable translational ordering is present, with the ester groups tending to line up in register.

Conclusion. There are several findings in the simulation that are of considerable interest with respect to the overall picture concerning the random copolyesters. First, it appears that the major difference between the high-temperature nematic phase, which shows diffuse X-ray scattering, and the ordered or crystalline lower temperature phase, which shows much sharper reflections, is the extreme intramolecular conformational disorder in the former. Second, it appears that

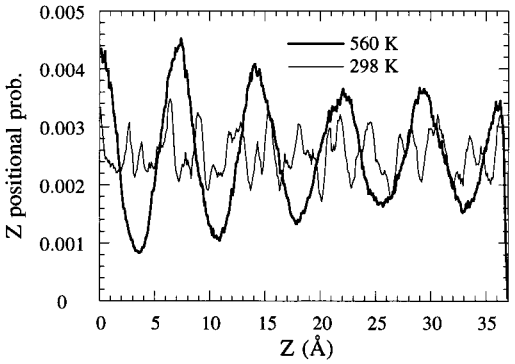

Figure 13. Translational register of chains. The probability that a selected ester group carbon has another ester group carbon in another chain displaced from it along the *c* direction by a distance *Z*. The thick curve is 560 K, and the thin curve is 298 K.

both phases show the presence of translational register. The ability for the random copolymers to develop such register has been a phenomenon that has inspired a great deal of effort directed toward its explanation. This situation occurs here in MD simulation where the structure appears to be able to explore the appropriate configuration space. Thus, the register would seem to be not only an accessible condition but the thermodynamically stable state.

Acknowledgment. We are indebted to the Polymer Program, Division of Materials Research of the National Science Foundation for financial support of this work. The Center for High Performance Computing (CHPC) at University of Utah is gratefully acknowledged for use of their facilities.

References and Notes

(1) (a) Biswas, A.; Blackwell, J. *Macromolecules* **1988**, *21*, 3146. (b) Biswas, A.; Blackwell, J. *Macromolecules* **1988**, *21*, 3152. (c) Biswas, A.; Blackwell, J. *Macromolecules* **1988**, *21*, 3158.
(2) Gutierrez, G. A.; Chivers, R. A.; Blackwell, J.; Stamatoff, J. B.; Yoon, H. *Polymer* **1983**, *24*, 937.
(3) Chivers, R. A.; Blackwell, J.; Gutierrez, G. A. *Polymer* **1984**, *25*, 435.
(4) (a) Butzbach, G. D.; Wendorff, J. H.; Zimmermann, H. J. *Makromol. Chem., Rapid Commun.* **1985**, *6*, 821. (b) Butzbach, G. D.; Wendorff, J. H.; Zimmermann, H. J. *Polymer* **1986**, *27*, 1337.
(5) Viney, C.; Mitchell; G. R.; Windle, A. H. *Mol. Cryst. Liq. Cryst.* **1985**, *129*, 75.
(6) Wilson, D. J.; Vonk, C. G.; Windle, A. H. *Polymer* **1992**, *34*, 227.
(7) Alhaj-Mohammed, M. H.; Davies, G. R.; Jawad, S. A.; Ward, I. M. *J. Polym. Sci. B* **1988**, *26*, 1751.
(8) Kalika, D. S.; Yoon, D. Y. *Macromolecules* **1991**, *24*, 3404.
(9) Chiou, J. S.; Paul, D. R. *J. Polym. Sci., Polym. Phys. Ed.* **1987**, *25*, 1699.
(10) (a) Weinkauf, D. H.; Paul, D. R. *J. Polym. Sci., Polym. Phys. Ed.* **1991**, *29*, 329. (b) Weinkauf, D. H.; Paul, D. R. *J. Polym. Sci., Polym. Phys. Ed.* **1992**, *30*, 817. (c) Weinkauf, D. H.; Paul, D. R. *J. Polym. Sci., Polym. Phys. Ed.* **1992**, *30*, 837.
(11) Miranda, N. R.; Willits, J. T.; Freeman, B. D.; Hopfenberg, H. B. *J. Membr. Sci.* **1994**, *94*, 67.
(12) Weinkauf, D. H.; Kim, H. D.; Paul, D. R. *Macromolecules* **1992**, *25*, 788.
(13) Hanna, S.; Windle, A. H. *Polymer* **1988**, *29*, 207.
(14) Jung, B.; Schurmann, B. L. *Macromolecules* **1989**, *22*, 477.
(15) Jung, B.; Schurmann, B. L. *Mol. Cryst. Liq. Cryst.* **1990**, *185*, 141.
(16) Rutledge, G. C. *Macromolecules* **1992**, *25*, 3995.
(17) Foulger, S. H.; Rutledge, G. C. *Macromolecules* **1995**, *28*, 7075.
(18) Huth, J.; Mosell, T.; Nicklas, K.; Sariban, A.; Brickmann, J. *J. Phys. Chem.* **1994**, *98*, 7685.
(19) Rutledge, G. C.; Suter, U. W. *Macromolecules* **1991**, *24*, 1921.
(20) Hofmann, D.; Schneider, A. I.; Blackwell, J. *Polymer* **1994**, *35*, 5604.
(21) Foulger, S. H.; Rutledge, G. C. *J. Polym. Sci., Part B: Polym. Phys.* **1998**, *36*, 727.
(22) Han, J.; Boyd, R. H. *Polymer* **1996**, *37*, 1797.
(23) Gee, R. H.; Boyd, R. H. *Polymer* **1995**, *36*, 1435.
(24) Han, J.; Boyd, R. H. *Macromolecules* **1994**, *27*, 5365.
(25) Pant, P. V. K.; Han, J.; Smith, G. D.; Boyd, R. H. *J. Chem. Phys.* **1993**, *99*, 597.
(26) Hedenqvist, M. S.; Bharadwaj, R.; Boyd, R. H. *Macromolecules* **1998**, *31*, 1556.
(27) Cao, M. Y.; Wunderlich, B. *J. Polym. Sci., Polym. Phys. Ed.* **1985**, *23*, 521.
(28) Adams, J. M.; Morsi, S. E. *Acta Crystallogr.* **1976**, *B32*, 1345.
(29) Hummel, J. P.; Flory, J. P. *Macromolecules* **1980**, *13*, 479.
(30) Coulter, P.; Windle, A. H. *Macromolecules* **1989**, *22*, 1129.
(31) Lautenschlager, P.; Brickmann, J.; van Ruiten, J.; Meier, R. J. *Macromolecules* **1991**, *24*, 1284.
(32) (a) Flory, P. J. *Statistical Mechanics of Chain Molecules*; Wiley: New York, 1969. (b) Flory, P. J.; Williams, A. D. *J. Polym. Sci., Polym. Phys. Ed.* **1967**, *5*, 399. (c)Williams, A. D.; Flory, P. J. *J. Polym. Sci., Polym. Phys. Ed.* **1967**, *5*, 417.
(33) Swope, W. C.; Andersen, H. C.; Berens, P. H.; Wilson, K. R. *J. Chem. Phys.* **1982**, *76*, 637.
(34) Verlet, L. *Phys. Rev.* **1967**, *159*, 98.
(35) Berendsen, H. J. C.; Potsma, J. P. M.; van Gunsteren, W. F.; DiNola, A.; Haak, J. R. *J. Chem. Phys.* **1984**, *81*, 3684.
(36) Allen, M. P.; Tildesley, D. J. *Computer Simulation of Liquids*; Clarendon Press: Oxford, 1987; Chapter 2.
(37) The MOLBD3 force field is available in the POLYMER module of the SYBYL simulation software of the Tripos Co., St. Louis, MO.
(38) Smith, G. D.; Boyd, R. H. *Macromolecules* **1990**, *23*, 1527.
(39) Sorensen, R. A.; Liau, W. B.; Kesner, L.; Boyd, R. H. *Maromolecules* **1988**, *21*, 200.
(40) Bharadwaj, R. K. Ph.D. Dissertation, University of Utah, Salt Lake City, UT, 1997.
(41) Block, H.; Walker, S. M. *Chem. Phys. Lett.* **1973**, *19*, 363.
(42) Ludovice, P. J.; Suter, U. W. In *Computational Modeling of Polymers*; Bicerano, J., Ed.; Marcel Dekker: New York, 1992.
(43) Smith, G. D.; Jaffe, R. L.; Yoon, D. Y. *Macromolecules* **1993**, *26*, 298.
(44) Smith, G. D.; Yoon, D. Y.; Jaffe, R. L.; Colby, R. L.; Krishnamoorti, R.; Fetters, L. J. *Macromolecules* **1996**, *29*, 3462.
(45) Engberg, K.; Stromberg, O.; Martinsson, Gedde, U. W. *Polym. Eng. Sci.* **1994**, *34*, 1336.
(46) Flores, A.; Ania, F.; Balta Calleja, F. J.; Ward, I. M. *Polymer* **1993**, *34*, 2915.
(47) van Krevelen, D. W.; Hoftyzer, P. J. *Properties of Polymers*; Elsevier: Amsterdam, The Netherlands, 1976.
(48) Porter, D. *Group Interaction Modelling of Polymer Properties*; Marcel Dekker: New York, 1995.
(49) Wagner, C. N. J. *J. Non-Cryst. Solids* **1978**, *31*, 1.
(50) Alexander, L. E. *X-ray Diffraction Methods in Polymer Science*; Wiley: New York, 1969.

MA9810565